Coherent manipulation of Andreev states in superconducting atomic contacts

— Source link ↗

Camille Janvier, L. Tosi, L. Tosi, Landry Bretheau ...+9 more authors

Institutions: Centre national de la recherche scientifique, Balseiro Institute

Related papers:

- Direct Microwave Measurement of Andreev-Bound-State Dynamics in a Semiconductor-Nanowire Josephson Junction.

- Exciting Andreev pairs in a superconducting atomic contact

- Spin-orbit splitting of Andreev states revealed by microwave spectroscopy

- Andreev level qubit.

- Signatures of Majorana Fermions in Hybrid Superconductor-Semiconductor Nanowire Devices

REPORTS

MESOSCOPIC PHYSICS

Coherent manipulation of Andreev states in superconducting atomic contacts

C. Janvier,[1] L. Tosi,[1,2] L. Bretheau,[1]* Ç. Ö. Girit,[1]† M. Stern,[1] P. Bertet,[1] P. Joyez,[1] D. Vion,[1] D. Esteve,[1] M. F. Goffman,[1] H. Pothier,[1] C. Urbina[1]‡

Coherent control of quantum states has been demonstrated in a variety of superconducting devices. In all of these devices, the variables that are manipulated are collective electromagnetic degrees of freedom: charge, superconducting phase, or flux. Here we demonstrate the coherent manipulation of a quantum system based on Andreev bound states, which are microscopic quasi-particle states inherent to superconducting weak links. Using a circuit quantum electrodynamics setup, we performed single-shot readout of this Andreev qubit. We determined its excited-state lifetime and coherence time to be in the microsecond range. Quantum jumps and parity switchings were observed in continuous measurements. In addition to having possible quantum information applications, such Andreev qubits are a test-bed for the physics of single elementary excitations in superconductors.

The ground state of a uniform superconductor is a many-body coherent state. Microscopic excitations of this superconducting condensate—which can be created, for example, by the absorption of photons with high-enough energy—are delocalized and incoherent because they have energies in a continuum of states. Localized states arise in situations where the superconducting gap Δ or the superconducting phase undergo strong spatial variations: examples include Shiba states around magnetic impurities (1) and Andreev states in vortices (2) or in weak links between two superconductors (3). Because they have discrete energies within the gap, Andreev states are expected to be amenable to coherent manipulation (4–8). In the simplest weak link, a single conduction channel that is shorter than the superconducting coherence length ξ, there are only two Andreev levels $\pm E_A(\tau/\delta) = \pm\Delta\sqrt{1 - \tau \sin^2(\delta/2)}$, which are governed by the transmission probability τ of electrons through the channel and the phase difference δ between the two superconducting condensates (3). Despite the absence of actual barriers, quasi-particles (bogoliubons) occupying these Andreev levels are localized over a distance $\sim\xi$ around the weak link by the gradient of the superconducting phase, and the system can be considered an Andreev quantum dot (5, 6). Figure 1 shows the energies $E_{g,o,e}(\delta)$ of the different states of this dot. In the spin-singlet ground state $|g\rangle$, only the negative-energy Andreev level is occupied and $E_g = -E_A$. If a single quasi-particle is added, the dot reaches a spin-degenerate odd-parity state $|o\rangle$ with $E_o = 0$ (9–12). Adding a second quasi-particle of opposite spin to the dot in state $|o\rangle$ brings it to a spin-singlet even-parity excited state $|e\rangle$ with $E_e = +E_A$ (13, 14). The $|e\rangle$ state can also be reached directly from $|g\rangle$ by absorption of a photon of energy $2E_A$. In this work, we demonstrate experimentally the ma-

nipulation of coherent superpositions of states $|g\rangle$ and $|e\rangle$, even if parasitic transitions to $|o\rangle$ are also observed.

Atomic-size contacts are suitable systems to address the Andreev physics because they accommodate a small number of short conduction channels (15). We create them using the microfabricated break-junction technique (16). Figure 2 presents the sample used in the experiment. An aluminum loop with a narrow suspended constriction (Fig. 2C) is fabricated on a polyimide flexible substrate mounted on a bending mechanism cooled down to ~30 mK (17). The substrate is first bent until the bridge breaks. Subsequent fine-tuning of the bending allows creating different atomic contacts and adjusting the transmission probability of their channels. The magnetic flux ϕ threading the loop controls the phase drop $\delta = 2\pi\phi/\phi_0$ (ϕ_0, flux quantum) across the contact and, thus, also controls the Andreev transition frequency $f_A(\tau,\delta) = 2E_A/h$ (h, Planck's constant). To excite and probe the Andreev dot, the loop is inductively coupled to a niobium quarter-wavelength microwave resonator (17) (Fig. 2B) in a circuit quantum electrodynamics architecture (18, 19). The resonator is probed by reflectometry at a frequency f_0 close to its bare resonance frequency $f_R \simeq 10.134$ GHz. The actual resonator frequency is different for each one of the three Andreev dot states: In the odd state, the resonance frequency is unaltered, whereas the two even states lead to opposite shifts around f_R (20). The Andreev transition $|g\rangle \rightarrow |e\rangle$ is driven by a second tone of frequency f_1. Details of the setup are shown in figs. S1 and S2 (20).

Here we present data obtained on a representative atomic contact containing only one high-transmission channel. Data from other contacts are shown in figs. S6 to S8. First, we performed pulsed two-tone spectroscopy by applying a 13-μs driving pulse of variable frequency, immediately followed by a 1-μs-long measurement pulse ($f_0 \simeq 10.1337$ GHz) probing the resonator with an
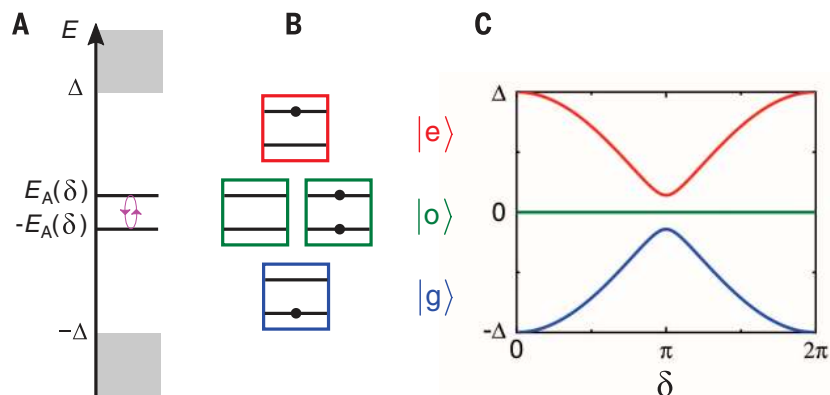
Fig. 1. Single-channel Andreev quantum dot. (**A**) Energy levels: Two discrete Andreev bound levels detach symmetrically from the upper and lower continua of states (light gray regions for $|E| > \Delta$). Photons of energy $2E_A$ can induce transitions between the two Andreev levels (magenta arrows). (**B**) Occupation of Andreev levels in the four possible quantum states of the Andreev dot. Only the lower Andreev level is occupied in the ground state $|g\rangle$ (blue box). In the excited state $|e\rangle$ (red box), only the upper Andreev bound level is occupied. In the doubly degenerate odd state $|o\rangle$, both Andreev levels are either occupied or empty. (**C**) Energy of the four Andreev dot states for a channel of transmission probability $\tau = 0.98$, as a function of the phase difference δ across the weak link.

[1]Quantronics Group, Service de Physique de l'État Condensé, CNRS UMR 3680, IRAMIS, CEA-Saclay, 91191 Gif-sur-Yvette, France. [2]Centro Atómico Bariloche and Instituto Balseiro, Comisión Nacional de Energía Atómica, 8400 Bariloche, Argentina.
*Present address: Department of Physics, Massachusetts Institute of Technology, Cambridge, MA 02215, USA. †Present address: USR 3573, CNRS, Collège de France, 11 Place Marcelin Berthelot, 75005 Paris, France. ‡Corresponding author. E-mail: cristian.urbina@cea.fr

amplitude corresponding to an average number of photons in the resonator $\bar{n} \simeq 30$ (Fig. 3A). Apart from the signal at $f_1 \simeq f_0$, the spectrum displays a resonance corresponding to the Andreev transition. The spectrum is periodic in flux, with period ϕ_0, which allowed us to calibrate the value of δ across the contact (fig. S3). Fits of the measured lines for different contacts with the analytical form of $f_A(\tau, \delta)$ provide the transmission probability τ of highly transmitting channels with up to five significant digits, as well as the superconducting gap $\Delta/h = 44.3$ GHz of the aluminum electrodes.

The coupling between the resonator and the Andreev dot is evident from the avoided crossing between the two modes observed in single-tone continuous-wave spectroscopy (Fig. 3B). Fitting the data with the predictions of a Jaynes-Cummings model (19, 20) yields $g/2\pi = 74$ MHz (g, coupling strength) at the two degeneracy points where $f_A = f_R$. Notably, the resonance of the bare resonator is also visible for all values of the phase, signaling that on the time scale of the measurement the Andreev dot is frequently in the odd state $|o\rangle$ (10, 12, 21).

Figure 3C shows the density plots of the reflected signal quadratures (I and Q) corresponding to sequences of 8000 measurement pulses taken at $\delta = \pi$, without (Fig. 3C, left panel) and with (right panel) a π driving pulse applied just before each measurement pulse. The results gather in three separate clouds of points, demonstrating that a single measurement pulse allows resolution of the dot state. The normalized number of points in each cloud is a direct measurement of the populations of the three states.

The two panels of Fig. 3C show the population transfer between the two even states induced by the driving pulse. Continuous measurement of the state of the Andreev dot in the absence of drive reveals the quantum jumps (22) between the two even states and the changes of parity that correspond to the trapping and untrapping of quasi-particles in the dot (Fig. 3D). The analysis (23) of this real-time trace yields a parity-switching rate of ~50 kHz (20).

The coherent manipulation at $\delta = \pi$ of the two-level system formed by $|g\rangle$ and $|e\rangle$ is illustrated in Fig. 4. Figure 4A shows the Rabi oscillations between $|g\rangle$ and $|e\rangle$ obtained by varying the duration of a driving pulse at frequency $f_1 = f_A(\tau, \pi)$ (movie S1). Figure 4B shows how the populations of $|g\rangle$ and $|e\rangle$ change when the driving-pulse frequency f_1 is swept across the Andreev frequency
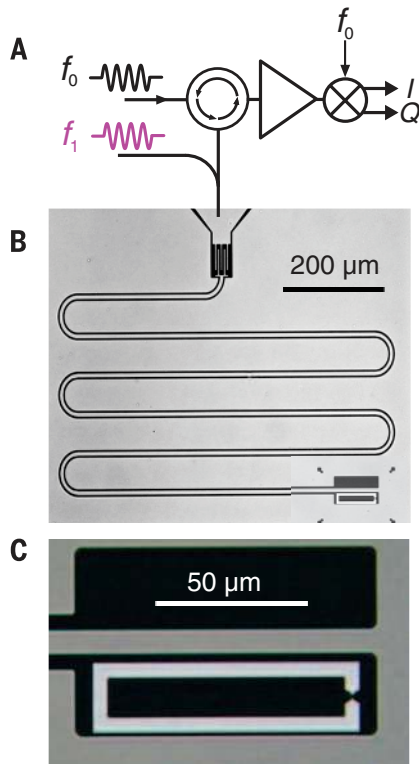
Fig. 2. Measurement setup of a superconducting atomic contact in a microwave resonator. (**A**) Simplified two-tone microwave setup. The measurement (frequency f_0) and drive (frequency f_1) signals are coupled to the resonator through the same port. After amplification, the reflected signal at f_0 is homodyne-detected by an IQ mixer, and its two quadratures (I and Q) are digitized. (**B**) Optical micrograph of the quarter-wavelength niobium coplanar meander resonator with an interdigitated capacitor $C \simeq 3$ fF at the coupling port. At the shorted end, an aluminum loop is inductively coupled to the resonator field. The resonator has resonance frequency $f_R \simeq 10.134$ GHz, with a total quality factor $Q = 2200$, close to critical coupling (see fig. S4). (**C**) Detailed view of the aluminum loop. Upon bending the substrate, the loop breaks at the narrow constriction to create an atomic contact.
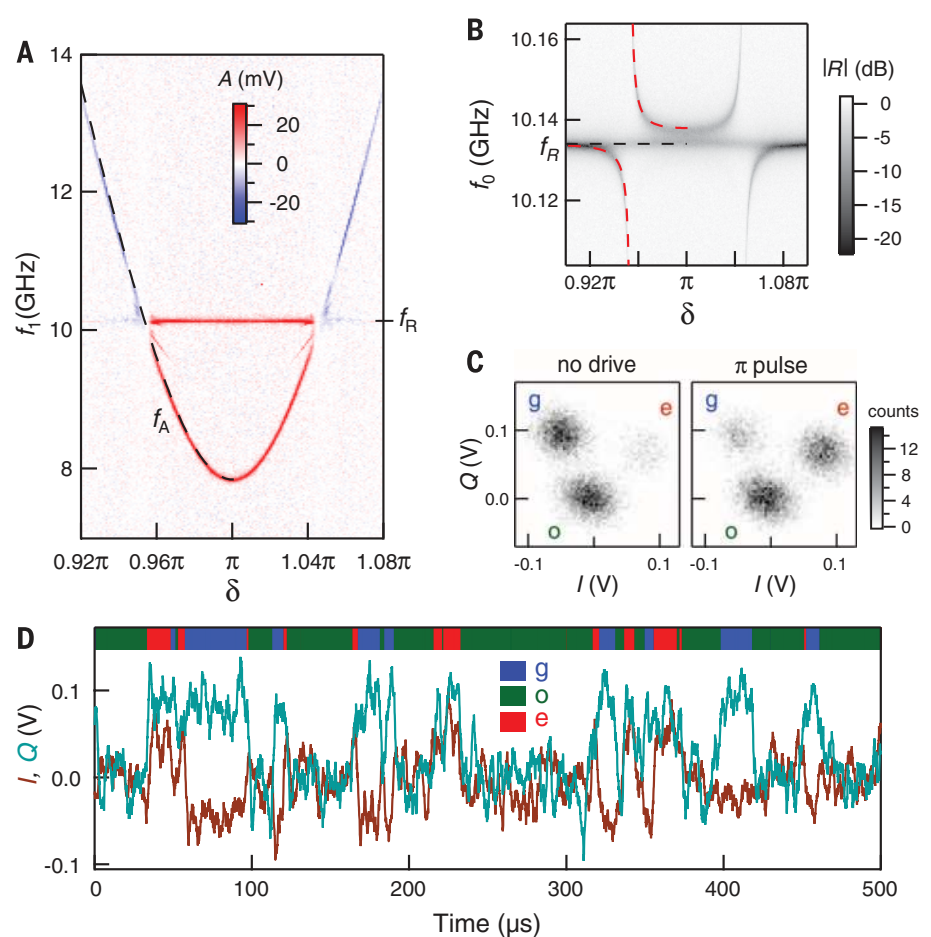

Fig. 3. Spectroscopy and quantum jumps. (**A**) Pulsed two-tone spectroscopy: color-coded amplitude A of one quadrature of reflected signal as a function of δ and f_1. The dashed black line shows the theoretical fit of Andreev transition frequency $f_A = 2E_A/h$ with $\tau = 0.99217$. A parasitic line, corresponding to a two-photon process $[2f_1 = f_R + f_A(\tau, \delta)]$, is visible just below 10 GHz. (**B**) Single-tone continuous-wave spectroscopy using a vector network analyzer (average number of photons in the resonator $\bar{n} \simeq 0.1$): resonator reflection amplitude $|R|$ as a function of δ and f_0. Red dashed curves correspond to fits of the anticrossings (20). Data aligned with the black dashed line correspond to the Andreev dot in state $|o\rangle$. (**C**) Density plots of I and Q quadratures at $\delta = \pi$ illustrate single-shot resolution of the quantum state of the dot. (Left) No drive at f_1. (Right) π pulse swapping the populations of $|g\rangle$ and $|e\rangle$. (**D**) Continuous measurement at $\delta = \pi$, with $\bar{n} \simeq 100$ and no driving signal. The brown (or cyan) time trace corresponds to the I (or Q) quadrature. The color (blue, green, or red) of the horizontal bar represents an estimate of the state (g, o, or e, respectively) found using a hidden Markov model toolbox (23).

$f_A(\tau,\pi)$. After a π pulse, the populations relax exponentially back to equilibrium with a relaxation time $T_1(\delta = \pi) \simeq 4$ μs (Fig. 4D). The Gaussian decay of detuned Ramsey fringes (Fig. 4F) provides a measurement of the coherence time $T_2^*(\delta = \pi) \simeq 38$ ns. This short coherence time is mainly due to low-frequency (i.e., lower-than-megahertz) fluctuations of the Andreev energy $E_A(\tau,\delta)$, as shown by the much longer decay time $T_2(\delta = \pi) \simeq 565$ ns $\gg T_2^*$ of a Hahn echo (Fig. 4G). Measurements at $\delta = \pi$ on other contacts with the same sample, with transmissions corresponding to a minimal Andreev frequency 3 GHz $< f_A(\tau,\pi) < 8$ GHz, give T_1 mostly around 4 μs (up to 8.5 μs), T_2^* around 40 ns (up to 180 ns), and T_2 around 1 μs (up to 1.8 μs), but no clear dependence of the characteristic times on τ is observed (figs. S7 and S8).

Figure 4E shows the measured relaxation rate $\Gamma_1 = 1/T_1$ as a function of the phase δ. The expected Purcell relaxation rate arising from the dissipative impedance seen by the atomic contact (light blue line in Fig. 4E) matches the experimental results only close to the degeneracy points where $f_A = f_R$ (vertical dotted lines) but is about five times smaller at $\delta = \pi$. On the basis of existing models, we estimate that relaxation rates due to quasi-particles (24–28) and phonons (7, 8, 21) are negligible. Empirically, we fit the data at $\delta = \pi$ by considering an additional phase-independent relaxation mechanism, which remains to be identified.

The linewidth of the spectroscopy line, which is a measure of the decoherence rate, shows a minimum at $\delta = \pi$ (Fig. 4C). The Gaussian decay of the Ramsey oscillations points to $1/f$ transmission fluctuations as the main source of decoherence at $\delta = \pi$, where the system is insensitive to flux noise to first order (28). Fluctuations of τ can arise from vibrations in the mechanical setup and from motion of atoms close to the contact. Figure 4C also shows the linewidths calculated, assuming $1/f$ transmission noise and both white and $1/f$ flux noise (20). The amplitude of the $1/f$ transmission noise, 2.5×10^{-6} Hz$^{-1/2}$ at 1 Hz, was adjusted to fit the measurement at $\delta = \pi$. The amplitudes of the white and $1/f$ flux noise were then obtained from a best fit of the linewidth phase dependence. The extracted $1/f$ noise amplitude (5 $\mu\phi_0$ Hz$^{-1/2}$ at 1 Hz) is a typical value for superconducting devices and has a negligible effect to second order (29). The source of the apparent white flux noise (48 nϕ_0 Hz$^{-1/2}$) has not yet been identified.

The Andreev quantum dot has been proposed as a new kind of superconducting qubit (5, 6), which differs markedly from existing ones (30). In qubits based on charge, flux, or phase (30), the states encoding quantum information correspond to collective electromagnetic modes, whereas in Andreev qubits they correspond to microscopic degrees of freedom of the superconducting condensate. Our results are a proof of concept of this new type of qubit. Further work is needed to fully understand the sources of decoherence and to couple several qubits in multichannel contacts (5, 8). With its parity sensitivity, the Andreev
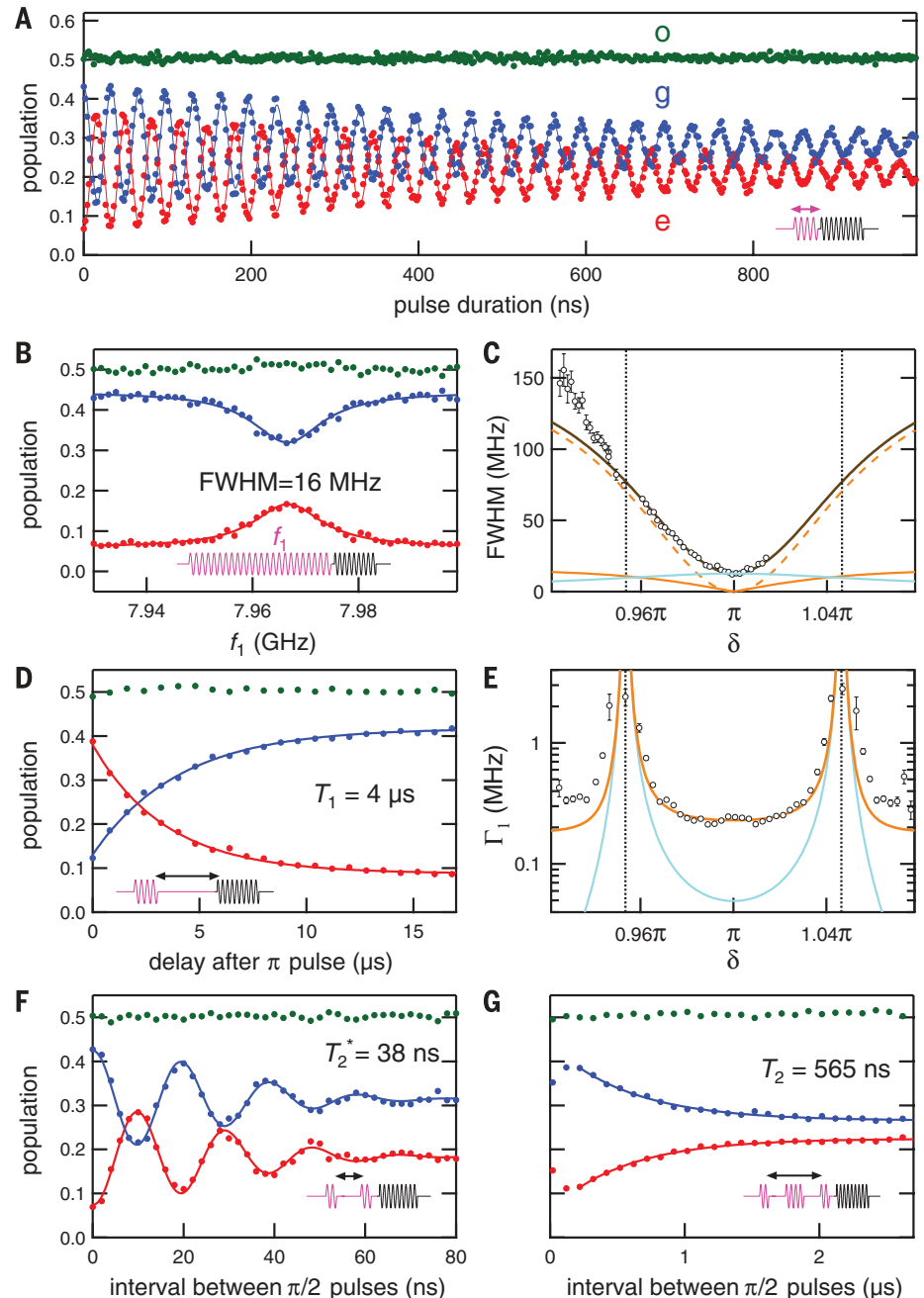
Fig. 4. Coherent manipulation of Andreev quantum dot states at $\delta = \pi$. Colored dots show measured populations: ground (blue), excited (red), and odd (green) states. Lines indicate theoretical fits. Sketches of pulse sequences for each type of measurement are shown in each panel (magenta, drive; black, measurement). (**A**) Rabi oscillations: populations as a function of the driving-pulse duration. (**B**) Spectroscopy: populations as a function of frequency f_1 of the saturating drive pulse. FWHM, full width at half maximum. (**C**) Phase dependence of the linewidth (FWHM) of the spectral line. Circles correspond to the result of a Lorentzian fit of the experimental resonances (20). The brown curve is the best fit to the data, including the contributions of $1/f$ transmission noise (light blue line) and both $1/f$ (orange line) and white flux noise (orange dashed line). (**D**) Relaxation of populations after a π driving pulse. (**E**) Phase dependence of relaxation rate $\Gamma_1 = 1/T_1$. Circles represent experimental data. The orange curve is the sum of the expected Purcell rate (light blue line) and an empirical phase-independent rate (180 kHz). In (C) and (E), vertical dotted lines indicate degeneracy points $f_A = f_R$. Error bars on circles denote uncertainties of the fits. (**F**) Ramsey fringes: populations as a function of delay between the two $\pi/2$ pulses detuned at $f_1 = f_A(\tau,\pi) + 51$ MHz. (**G**) Hahn echo: populations as a function of delay between the two $\pi/2$ pulses with a π pulse in between.

quantum dot is also a powerful tool to investigate quasi-particle–related limitations on the performance of superconducting qubits (28, 31, 32) and detectors (33). Furthermore, our experimental strategy could be used to explore hybrid superconducting devices in the regime where Andreev states evolve into Majorana states (34–36).

REFERENCES AND NOTES

1. K. J. Franke, G. Schulze, J. I. Pascual, *Science* **332**, 940–944 (2011).
2. C. Caroli, P. G. de Gennes, J. Matricon, *Phys. Lett.* **9**, 307–309 (1964).
3. C. W. J. Beenakker, H. van Houten, *Phys. Rev. Lett.* **66**, 3056–3059 (1991).
4. M. A. Despósito, A. Levy Yeyati, *Phys. Rev. B* **64**, 140511(R) (2001).
5. A. Zazunov, V. S. Shumeiko, E. N. Bratus', J. Lantz, G. Wendin, *Phys. Rev. Lett.* **90**, 087003 (2003).
6. N. M. Chtchelkatchev, Yu. V. Nazarov, *Phys. Rev. Lett.* **90**, 226806 (2003).
7. A. Zazunov, V. S. Shumeiko, G. Wendin, E. N. Bratus', *Phys. Rev. B* **71**, 214505 (2005).
8. C. Padurariu, Yu. V. Nazarov, *Europhys. Lett.* **100**, 57006 (2012).
9. J.-D. Pillet et al., *Nat. Phys.* **6**, 965–969 (2010).
10. M. Zgirski et al., *Phys. Rev. Lett.* **106**, 257003 (2011).
11. E. M. Levenson-Falk, F. Kos, R. Vijay, L. Glazman, I. Siddiqi, *Phys. Rev. Lett.* **112**, 047002 (2014).
12. A. Zazunov, A. Brunetti, A. Levy Yeyati, R. Egger, *Phys. Rev. B* **90**, 104508 (2014).
13. L. Bretheau, Ç. Ö. Girit, H. Pothier, D. Esteve, C. Urbina, *Nature* **499**, 312–315 (2013).
14. L. Bretheau, Ç. Ö. Girit, C. Urbina, D. Esteve, H. Pothier, *Phys. Rev. X* **3**, 041034 (2013).
15. E. Scheer, P. Joyez, D. Esteve, C. Urbina, M. H. Devoret, *Phys. Rev. Lett.* **78**, 3535–3538 (1997).
16. J. M. van Ruitenbeek et al., *Rev. Sci. Instrum.* **67**, 108 (1996).
17. C. Janvier et al., *J. Phys. Condens. Matter* **26**, 474208 (2014).
18. A. Wallraff et al., *Nature* **431**, 162–167 (2004).
19. G. Romero, I. Lizuain, V. S. Shumeiko, E. Solano, F. S. Bergeret, *Phys. Rev. B* **85**, 180506 (2012).
20. Materials and methods are available as supplementary materials on *Science* Online.
21. D. G. Olivares et al., *Phys. Rev. B* **89**, 104504 (2014).
22. R. Vijay, D. H. Slichter, I. Siddiqi, *Phys. Rev. Lett.* **106**, 110502 (2011).
23. M. Greenfield, D. S. Pavlichin, H. Mabuchi, D. Herschlag, *PLOS ONE* **7**, e30024 (2012).
24. J. M. Martinis, M. Ansmann, J. Aumentado, *Phys. Rev. Lett.* **103**, 097002 (2009).
25. G. Catelani, R. J. Schoelkopf, M. H. Devoret, L. I. Glazman, *Phys. Rev. B* **84**, 064517 (2011).
26. F. Kos, S. E. Nigg, L. I. Glazman, *Phys. Rev. B* **87**, 174521 (2013).
27. I. M. Pop et al., *Nature* **508**, 369–372 (2014).
28. C. Wang et al., *Nat. Commun.* **5**, 5836 (2014).
29. Y. Makhlin, A. Shnirman, *Phys. Rev. Lett.* **92**, 178301 (2004).
30. J. Clarke, F. K. Wilhelm, *Nature* **453**, 1031–1042 (2008).
31. U. Vool et al., *Phys. Rev. Lett.* **113**, 247001 (2014).
32. D. Ristè et al., *Nat. Commun.* **4**, 1913 (2013).
33. P. J. de Visser et al., *Phys. Rev. Lett.* **106**, 167004 (2011).
34. W. Chang, V. E. Manucharyan, T. S. Jespersen, J. Nygård, C. M. Marcus, *Phys. Rev. Lett.* **110**, 217005 (2013).
35. V. Mourik et al., *Science* **336**, 1003–1007 (2012).
36. D. Chevallier, P. Simon, C. Bena, *Phys. Rev. B* **88**, 165401 (2013).

CRITICAL PHENOMENA

Critical behavior at a dynamic vortex insulator-to-metal transition

Nicola Poccia,[1,2] Tatyana I. Baturina,[3,4,5] Francesco Coneri,[1] Cor G. Molenaar,[1] X. Renshaw Wang,[1] Ginestra Bianconi,[6] Alexander Brinkman,[1] Hans Hilgenkamp,[1] Alexander A. Golubov,[1,7] Valerii M. Vinokur[5]*

An array of superconducting islands placed on a normal metal film offers a tunable realization of nanopatterned superconductivity. This system enables investigation of the nature of competing vortex states and phase transitions between them. A square array creates the eggcrate potential in which magnetic field–induced vortices are frozen into a vortex insulator. We observed a vortex insulator–vortex metal transition driven by the applied electric current and determined critical exponents that coincided with those for thermodynamic liquid-gas transition. Our findings offer a comprehensive description of dynamic critical behavior and establish a deep connection between equilibrium and nonequilibrium phase transitions.

C ritical behaviors near phase transitions can be classified into universality classes determined only by a few properties characterizing the system, such as space dimensionality, range of interaction, and symmetry (1, 2). A paradigmatic concept of universality brought deep understanding of equilibrium critical phenomena [see, e.g., (3) and references therein]. Phase transitions and criticality far from equilibrium are less well understood. The experimental evidence for universality of nonequilibrium phase transitions is still scarce, calling for intensified experimental efforts.

Superconducting vortices offer a unique tunable laboratory for studying classical critical dynamics. To that end, we prepared an array of superconducting islands where vortices are pinned between the islands in the areas of weaker proximity-induced superconductivity—that is, at the energy dimples of an eggcrate potential (4). If thermal fluctuations are not strong enough to overcome the combined localizing action of mutual repulsion and pinning, vortices form the so-called vortex Mott insulating state at commensurate

fields corresponding to an integer number of vortices per pinning site (5). The predicted vortex Mott state seen in experiments on antidot arrays in superconducting films (6, 7) was conclusively confirmed in (8). In our experiment, performed in a classical regime, varying the magnetic field provides precise control over the vortex density and tunes the ratio of the vortex repulsion to the mobility, enabling the observation of a vortex insulator-to-metal transition.

Each of our samples consists of a 40-nm Au layer, patterned as a four-point setup in a van der Pauw configuration for transport measurements, on a Si/SiO_2 substrate (9). The Au pattern is overlaid with a square array of superconducting niobium (Nb) islands 45 nm thick. An array contains 90,000 Nb islands placed with a period $a = 267$ nm. The diameter of an island is 220 ± 3 nm and the island separation is 47 ± 3 nm. Shown in Fig. 1, A to D, are scanning electron microscopy (SEM), atomic force microscopy (AFM), and optical images of a sample and the height profile along one of the principal axes of the array. The superconducting transition temperature of the array, determined as the midpoint of the temperature resistance curve in the upper inset in Fig. 1A, is $T_c = 7.3$ K, which is 2 K lower than that of bulk Nb ($T_{c0} = 9.3$ K). This implies that the array is a strongly coupled network of superconducting islands (10–12). The parameters of our array ensure that the intersite barriers are high enough to provide pinning sufficient for formation of the vortex Mott insulator state and that vortex motion is thermally activated.

The measurements are carried out in a shielded cryostat at temperature $T = 1.4$ K. Figure 2A shows

[1]MESA+ Institute for Nanotechnology, University of Twente, 7500 AE Enschede, Netherlands. [2]Rome International Center for Materials Science Superstripes (RICMASS), Via dei Sabelli 119A, 00185 Roma, Italy. [3]A. V. Rzhanov Institute of Semiconductor Physics, Siberian Branch of the Russian Academy of Sciences, Novosibirsk 630090, Russia. [4]Novosibirsk State University, Novosibirsk 630090, Russia. [5]Materials Science Division, Argonne National Laboratory, Argonne, IL 60637, USA. [6]School of Mathematical Sciences, Queen Mary University of London, London E1 4NS, UK. [7]Moscow Institute of Physics and Technology, Dolgoprudnyi, Moscow District, Russia.
*Corresponding author. E-mail: vinokur@anl.gov